

The following resources related to this article are available online at www.sciencemag.org (this information is current as of September 7, 2009):

Updated information and services, including high-resolution figures, can be found in the online version of this article at:

<http://www.sciencemag.org/cgi/content/full/320/5876/634>

This article **cites 9 articles**, 2 of which can be accessed for free:

<http://www.sciencemag.org/cgi/content/full/320/5876/634#otherarticles>

This article has been **cited by** 61 article(s) on the ISI Web of Science.

This article has been **cited by** 2 articles hosted by HighWire Press; see:

<http://www.sciencemag.org/cgi/content/full/320/5876/634#otherarticles>

This article appears in the following **subject collections**:

Materials Science

http://www.sciencemag.org/cgi/collection/mat_sci

Information about obtaining **reprints** of this article or about obtaining **permission to reproduce this article** in whole or in part can be found at:

<http://www.sciencemag.org/about/permissions.dtl>

18. A. C. Yu, D. Margoliash, *Science* **273**, 1871 (1996).
 19. Z. Chi, D. Margoliash, *Neuron* **32**, 899 (2001).
 20. R. H. Hahnloser, A. A. Kozhevnikov, M. S. Fee, *Nature* **419**, 65 (2002).
 21. A. Leonardo, M. S. Fee, *J. Neurosci.* **25**, 652 (2005).
 22. S. W. Bottjer, K. A. Halsema, S. A. Brown, E. A. Miesner, *J. Comp. Neurol.* **279**, 312 (1989).
 23. M. A. Farries, D. J. Perkel, *J. Neurosci.* **22**, 3776 (2002).
 24. S. W. Bottjer, E. A. Miesner, A. P. Arnold, *Science* **224**, 901 (1984).
 25. C. Scharff, F. Nottebohm, *J. Neurosci.* **11**, 2896 (1991).
 26. M. H. Kao, A. J. Doupe, M. S. Brainard, *Nature* **433**, 638 (2005).
 27. B. P. Ölveczky, A. S. Andalman, M. S. Fee, *PLoS Biol.* **3**, e153 (2005).
 28. K. Doya, T. J. Sejnowski, in *Advances in Neural Information Processing Systems*, G. Tesauro, D. S. Touretzky, T. K. Leen, Eds. (MIT Press, Cambridge, MA, 1995), vol. 7, pp. 101–108.
29. T. W. Troyer, S. W. Bottjer, *Curr. Opin. Neurobiol.* **11**, 721 (2001).
 30. J. A. Thompson, F. Johnson, *Dev. Neurobiol.* **67**, 205 (2007).
 31. See supporting material on Science Online.
 32. O. Tchernichovski, F. Nottebohm, C. E. Ho, B. Pesaran, P. P. Mitra, *Anim. Behav.* **59**, 1167 (2000).
 33. S. Deregnacourt, P. P. Mitra, O. Feher, C. Pytte, O. Tchernichovski, *Nature* **433**, 710 (2005).
 34. N. Fujii, A. M. Graybiel, *Science* **301**, 1246 (2003).
 35. M. S. Fee, A. A. Kozhevnikov, R. H. Hahnloser, *Ann. N.Y. Acad. Sci.* **1016**, 153 (2004).
 36. A. Alvarez-Buylla, C. Y. Ling, F. Nottebohm, *J. Neurobiol.* **23**, 396 (1992).
 37. R. Mooney, *J. Neurosci.* **12**, 2464 (1992).
 38. R. Mooney, M. Rao, *J. Neurosci.* **14**, 6532 (1994).
 39. K. Herrmann, A. P. Arnold, *J. Neurosci.* **11**, 2063 (1991).
 40. E. Akutagawa, M. Konishi, *Proc. Natl. Acad. Sci. U.S.A.* **91**, 12413 (1994).
 41. J. M. Kittelberger, R. Mooney, *J. Neurosci.* **19**, 9385 (1999).
 42. L. L. Stark, D. J. Perkel, *J. Neurosci.* **19**, 9107 (1999).
43. G. M. Edelman, *Neural Darwinism: The Theory of Neuronal Group Selection* (Basic Books, New York, 1987).
 44. O. Sporns, G. M. Edelman, *Child Dev.* **64**, 960 (1993).
 45. P. Marler, *J. Neurobiol.* **33**, 501 (1997).
 46. M. Hadders-Algra, *Dev. Med. Child Neurol.* **42**, 566 (2000).
 47. We thank A. Graybiel, E. Bizzi, and J. Goldberg for comments on the manuscript and F. Nottebohm for helpful discussion regarding HVC lesions. Supported by NIH grant MH067105, a Hertz Foundation Silvio Micali fellowship (D.A.), and a Friends of the McGovern Institute fellowship (A.S.A.).

Supporting Online Material

www.sciencemag.org/cgi/content/full/320/5876/630/DC1

Materials and Methods

SOM Text

Figs. S1 to S5

Sounds S1 to S6

References

11 January 2008; accepted 24 March 2008

10.1126/science.1155140

High-Thermoelectric Performance of Nanostructured Bismuth Antimony Telluride Bulk Alloys

Bed Poudel,^{1,2*} Qing Hao,^{3*} Yi Ma,^{1,2} Yucheng Lan,¹ Austin Minnich,³ Bo Yu,¹ Xiao Yan,¹ Dezhi Wang,¹ Andrew Muto,³ Daryoosh Vashaee,³ Xiaoyuan Chen,³ Junming Liu,⁴ Mildred S. Dresselhaus,⁵ Gang Chen,^{3†} Zhifeng Ren^{1†}

The dimensionless thermoelectric figure of merit (ZT) in bismuth antimony telluride (BiSbTe) bulk alloys has remained around 1 for more than 50 years. We show that a peak ZT of 1.4 at 100°C can be achieved in a p-type nanocrystalline BiSbTe bulk alloy. These nanocrystalline bulk materials were made by hot pressing nanopowders that were ball-milled from crystalline ingots under inert conditions. Electrical transport measurements, coupled with microstructure studies and modeling, show that the ZT improvement is the result of low thermal conductivity caused by the increased phonon scattering by grain boundaries and defects. More importantly, ZT is about 1.2 at room temperature and 0.8 at 250°C, which makes these materials useful for cooling and power generation. Cooling devices that use these materials have produced high-temperature differences of 86°, 106°, and 119°C with hot-side temperatures set at 50°, 100°, and 150°C, respectively. This discovery sets the stage for use of a new nanocomposite approach in developing high-performance low-cost bulk thermoelectric materials.

Solid-state cooling and power generation based on thermoelectric effects have potential applications in waste-heat recovery, air conditioning, and refrigeration. The efficiency of thermoelectric devices is determined by the materials' dimensionless figure of merit, defined as $ZT = (S^2\sigma/k)T$, where S , σ , k , and T are the Seebeck coefficient, electrical conductivity, thermal conductivity, and absolute temperature, respectively (1–3). An average ZT in the

application temperature range must be higher than 1 to make a thermoelectric device competitive (1–3).

There have been persistent efforts to improve ZT values since the 1950s, but the peak ZT of dominant commercial materials based on Bi₂Te₃ and its alloys, such as Bi_xSb_{2-x}Te₃ (p-type), has remained at 1. During the past decade, several groups have reported enhanced ZT in (i) superlattices such as Bi₂Te₃/Sb₂Te₃ (4) and PbSe_{0.98}Te_{0.02}/PbTe (5), because of reductions in the lattice thermal conductivity, and (ii) new bulk materials, such as lead antimony silver telluride (LAST) and its alloys (6), including skutterudites (7). Although high ZT values were reported in superlattice structures, it has proven difficult to use them in large-scale energy-conversion applications because of limitations in both heat transfer and cost. Bulk materials with improved ZT, such as LAST and skutterudites, are ideal for high-temperature operations. However, at rela-

tively near room temperature (0° to 250°C), Bi₂Te₃-based materials still dominate.

We have pursued an approach in which the primary cause of ZT enhancement in superlattices—reduced thermal conductivity—also exists in random nanostructures (8, 9). We report a substantial ZT increase in bulk materials made from nanocrystalline (NC) powders of p-type Bi_xSb_{2-x}Te₃, reaching a peak ZT of 1.4 at 100°C. The enhanced ZT is the result of a significant reduction in thermal conductivity caused by strong phonon scattering by interfaces in the nanostructures. There have also been reports of ZT improvements at room temperature in Bi₂Te₃-based materials caused by the addition of Bi₂Te₃ nanotubes (10) and by melt spinning (11).

Our method, on the other hand, is based on the ball milling and hot pressing of nanoparticles into bulk ingots. This approach is simple, is cost effective, and can be used on other materials. Our materials have a ZT of about 1.2 at room temperature and 0.8 at 250°C with a peak of 1.4 at 100°C. In comparison, conventional Bi₂Te₃-based materials have a peak ZT of about 1 at room temperature and about 0.25 at 250°C. The high ZT in the 25° to 250°C temperature range makes the NC bulk materials attractive for cooling and low-grade waste-heat recovery applications. The materials can also be integrated into segmented thermoelectric devices for thermoelectric power generation that operate at high temperatures. In addition to the high ZT values, the NC bulk materials are also isotropic. They do not suffer from the cleavage problem that is common in traditional zone melting—made ingots, which leads to easier device fabrication and system integration and to a potentially longer device lifetime.

Sample preparation. Nanopowders were made by ball milling bulk p-type BiSbTe alloy ingots (12). Bulk disk samples (1.25 to 2.5 cm in diameter and 2 to 15 mm in thickness) were made by hot pressing the nanopowders loaded in 1.25- to 2.5-cm (inner diameter) graphite dies (12). Disks (1.25 cm in diameter and 2 mm in thickness) and bars (about 2 mm by 2 mm by

¹Department of Physics, Boston College, Chestnut Hill, MA 02467, USA. ²GMZ Energy, Incorporated, 12A Hawthorn Street, Newton, MA 02458, USA. ³Department of Mechanical Engineering, Massachusetts Institute of Technology (MIT), Cambridge, MA 02139, USA. ⁴Laboratory of Solid State Microstructures and Department of Physics, Nanjing University, China. ⁵Department of Physics and Department of Electrical Engineering and Computer Science, MIT, Cambridge, MA 02139, USA.

*These authors contributed equally to this work.

†To whom correspondence should be addressed. E-mail: gchen2@mit.edu (G.C.); renzh@bc.edu (Z.R.)

12 mm) were cut from both the axial and disk plane directions. The disks and bars were also polished for σ , k , and S measurements.

To achieve high ZT, researchers must control the size and quality of the starting nanoparticles. For good electrical conductivity, it is especially

important to prevent oxidation. Figure 1 shows the x-ray diffraction (XRD) pattern (Fig. 1A), the scanning electron microscope (SEM) image (Fig. 1B), and the low- and high-magnification transmission electron microscope (TEM) images (Fig. 1, C and D) of the nanopowders after ball-

milling. The XRD patterns verify that the powder is in a single phase and is well matched with $\text{Bi}_{0.5}\text{Sb}_{1.5}\text{Te}_3$. The broadened diffraction peaks indicate that the particles are small, which is also confirmed in the SEM image (Fig. 1B) and the low-magnification TEM image (Fig. 1C). The TEM image (Fig. 1C) also shows that the nanoparticles have sizes ranging up to 50 nm, with an average size of about 20 nm. The high-resolution TEM image (Fig. 1D) confirms the excellent crystallinity of the nanoparticles and the clean surfaces. The inset in Fig. 1D also shows that some of the nanoparticles are even smaller than 5 nm.

Transport properties. The temperature dependences of several key properties of a typical NC bulk sample are compared in Fig. 2 with those of the state-of-the-art (SOA) p-type BiSbTe alloy ingot. All of the properties were measured in the same direction and reproduced on about 100 samples. The electrical conductivity of the NC bulk sample is slightly higher than that of the SOA ingot (Fig. 2A), but the Seebeck coefficient of the bulk sample is either slightly lower or higher than that of the ingot, depending on its temperature (Fig. 2B). Ultimately, the power factor ($S^2\sigma$) values of the bulk sample are similar to or higher than those of an ingot at temperatures below 50°C and above 75°C, respectively (Fig. 2C).

We also found that the thermal conductivity of the NC bulk samples is significantly lower than that of the ingot and, more importantly, that the difference increases with increasing temperature (Fig. 2D), which leads to significantly enhanced ZT values (Fig. 2E) in the 20° to 250°C temperature range. It also shows that the peak ZT value shifts to a higher temperature (100°C). The peak ZT of the NC bulk samples is about

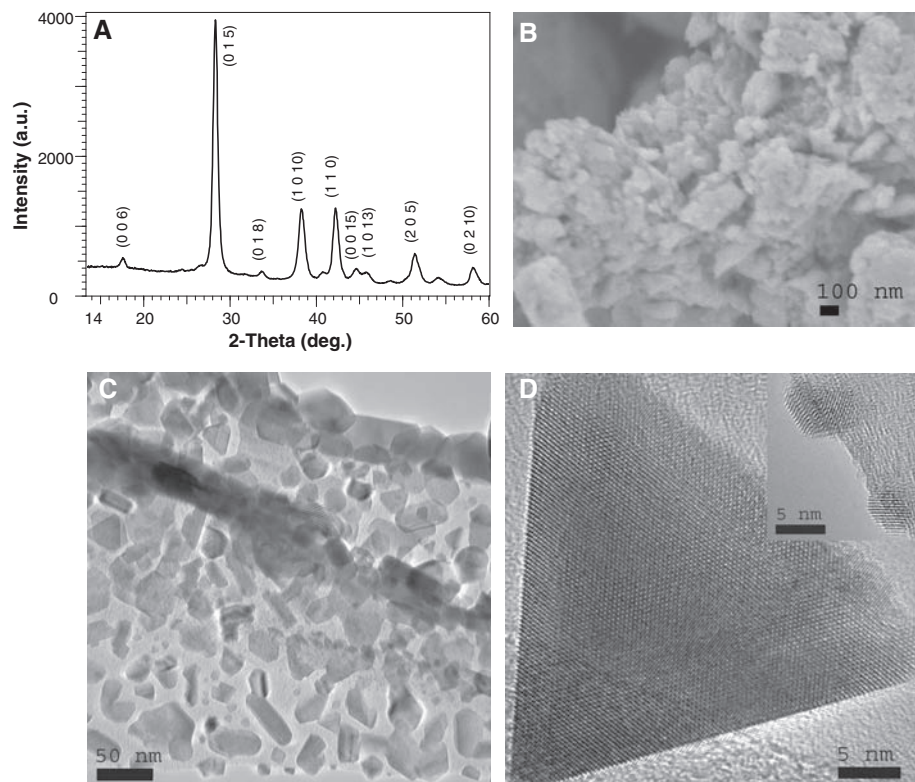


Fig. 1. XRD (A), SEM (B), low-magnification TEM (C), and high-magnification TEM (D) images of an as-ball-milled nanopowder. a.u., arbitrary units.

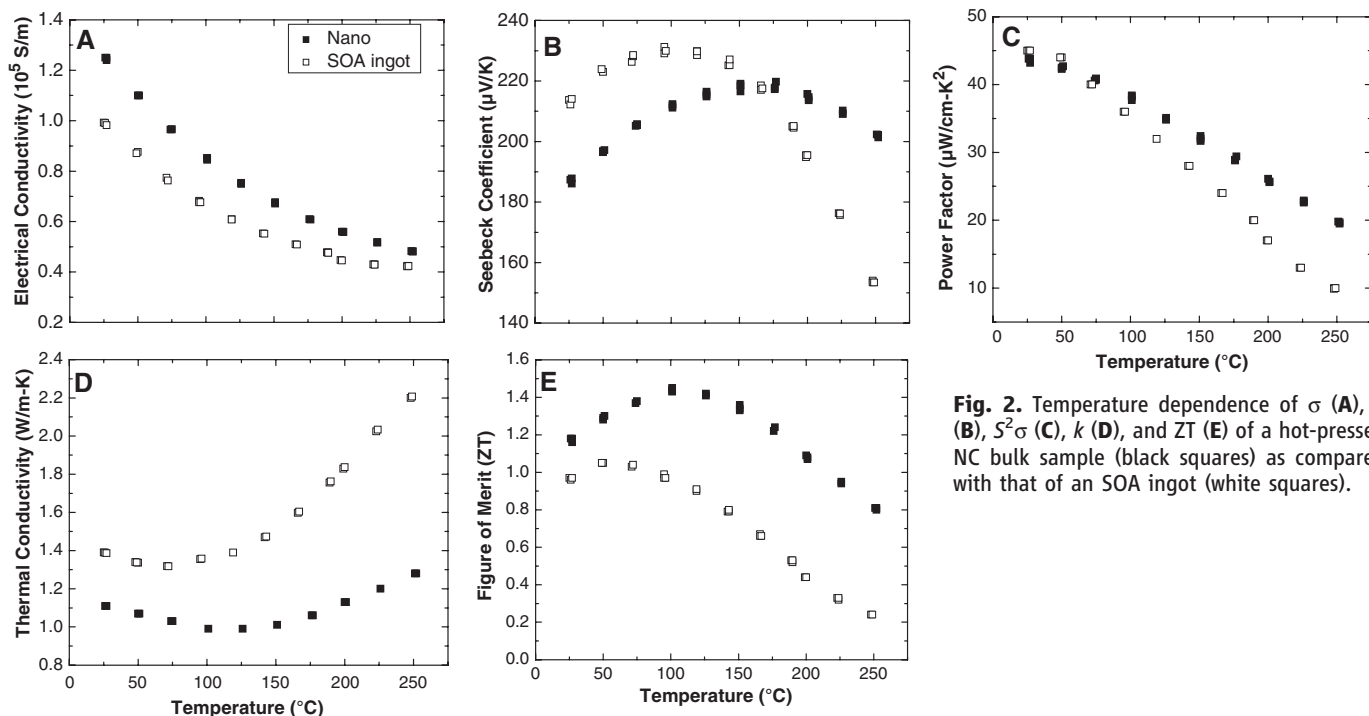


Fig. 2. Temperature dependence of σ (A), S (B), $S^2\sigma$ (C), k (D), and ZT (E) of a hot-pressed NC bulk sample (black squares) as compared with that of an SOA ingot (white squares).

1.4 at 100°C, which is significantly greater than that of the SOA Bi₂Te₃-based alloys. The ZT value of the SOA ingot starts to drop above 75°C and is below 0.25 at 250°C, whereas the ZT values for the NC bulk samples are still above 0.8 at 250°C. Such ZT characteristics are suitable for power generation applications because of a lack of available materials with high ZT in this temperature range.

All of these measurements were confirmed by two independent techniques on more than 100 samples. The electrical conductivity was measured by a four-point current-switching technique. We measured the Seebeck coefficient by a static dc method based on the slope of a voltage versus temperature-difference curve, using commercial equipment (ZEM-3, Ulvac, Inc., Methuen, Massachusetts, USA) on the same bar-type sample with a cross-sectional dimension of 2 mm by 2 mm and a length of 12 mm. The properties in the same sample were also measured by a home-built system, and the two sets of measurements are within 5% of each other.

We first measured the thermal diffusivity α by a laser-flash method on a disk using a commercial system (Netzsch Instruments, Inc., Burlington, Massachusetts, USA). After the measurement, bars were diced from the disks and α values were measured via the Ångström method in the

same home-built system. The α values from the bar and the disk agree within a range of 5%.

The thermal conductivity was calculated via the equation $k = \alpha\rho c_p$, where ρ is the density and c_p is the specific heat of the material that was measured with a differential scanning calorimeter (Netzsch Instruments, Inc.). To further check the property isotropy of the NC bulk samples, we cut disks and bars along and perpendicular to the press direction and then performed the measurements. Although individual properties may differ by 5% within the two directions, the final ZT values are isotropic. Such nearly isotropic characteristics are the result of the random orientation of the nanograins, showing that our NC bulk materials are superior to zone melting-made SOA Bi₂Te₃-based alloys, which have layered structures and, consequently, anisotropic thermoelectric properties. The highest ZT of the zone melting-made materials is along the basal plane of the crystal, but unfortunately this direction is vulnerable to cleavage, resulting in a difficult and low-yield module fabrication process.

For cooling applications, the stability of the nanostructures should not be a serious concern. High-temperature stability testing on the current NC bulk materials by repeated measurements up to 250°C did not show any sign of degradation,

suggesting potential power generation applications for waste-heat recovery in the reported temperature range.

Microstructure of NC bulk ingots. Detailed microstructure studies by TEM were carried out on NC bulk samples. The TEM specimens were prepared by dicing, polishing, and ion milling the bulk samples (13). Figure 3 shows the main structural features that we observed. In general, most of the grains are nanosized (Fig. 3, A and B). Furthermore, these nanograins are highly crystalline, are completely random (large angles between adjacent lattice planes), and have very clean boundaries between grains. They are also closely packed (Fig. 3B), which is consistent with our full density measurements. We also observed some larger grains (Fig. 3C). However, under high-resolution TEM observation, these grains consist of 2- to 10-nm-sized nanodots with fuzzy boundaries (Fig. 3D). Usually, these nanodots are Sb-rich with a typical composition close to that of Bi:Sb:Te = 8:44:48, with Sb substituted for Te.

Although some of the nanodots are without boundaries (Fig. 3D), we found other nanodots that make small-angle boundaries with the matrix (Fig. 3E). In addition, we also observed pure Te precipitates ranging from 5 to 30 nm in size (Fig. 3F). The selected-area electron diffraction (SAED) pattern (Fig. 3F, inset) confirms the presence of

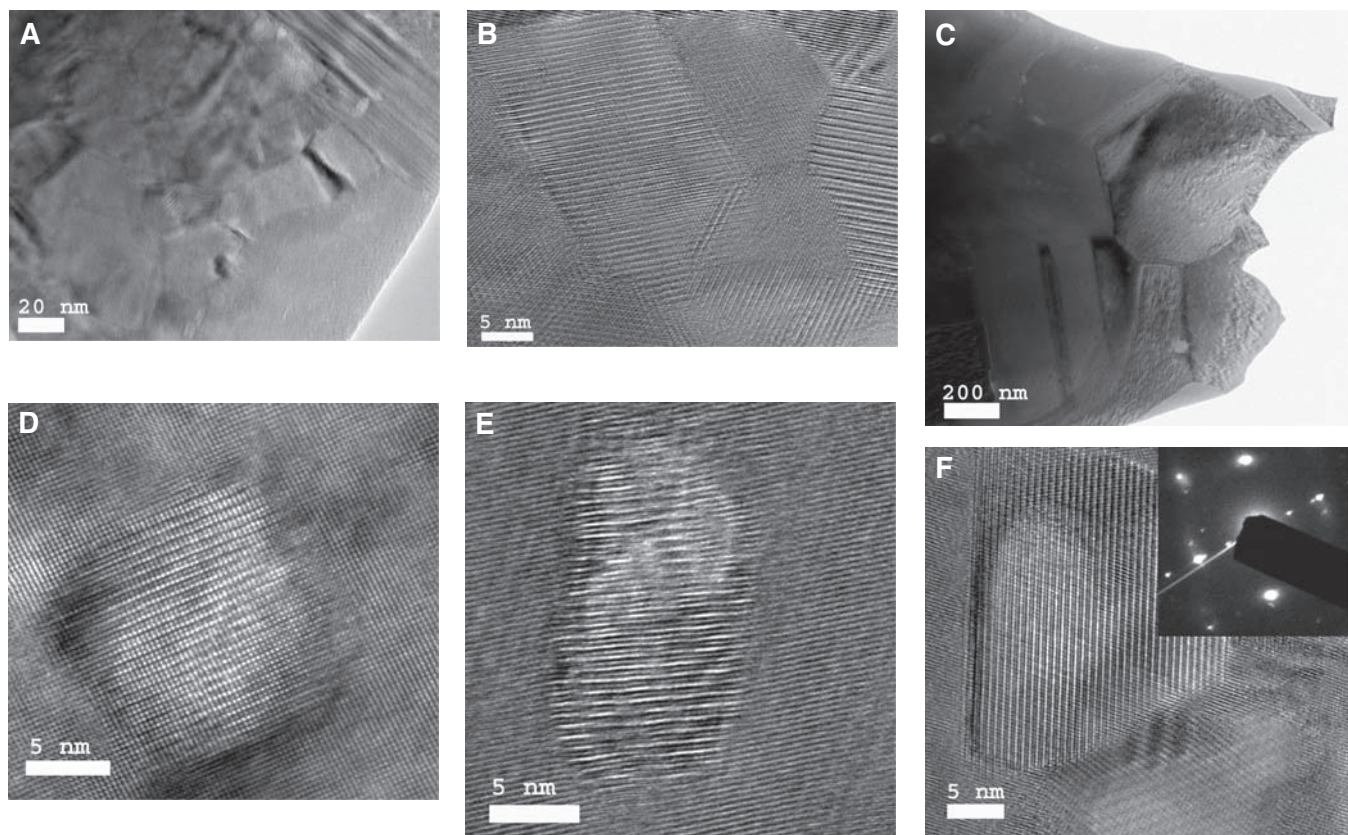


Fig. 3. TEM images showing the microstructures of a hot-pressed NC bulk sample. (A) Low-magnification image showing the nanograins. (B) High-magnification image showing the nanosize, high crystallinity, random orientation, and clean grain boundaries. (C) Low-magnification image showing

larger grains. (D and E) High-magnification images showing the nanodots in the matrix without boundaries (D) and with small-angle grain boundaries (E). (F) High-magnification image showing Te precipitate in the matrix. SAED pattern (inset) shows the Te phase of the precipitated nanodot in the matrix.

this Te phase. Generally speaking, nanodots can be found within a 50-nm-diameter area.

We speculate that these nanodots could be formed during the hot-press heating and cooling processes. Similar types of nanodots have been observed in LAST alloys and were allegedly responsible for the ZT enhancement in those alloys (6). However, because there are so many interfaces from nanograins in our material, nanodots may not be the only reason for the strong phonon scattering. The larger-sized grains containing nanodots (Fig. 3C) are likely to be the result of the nonuniform ball milling of the ingot and may have experienced some grain growth during the hot-press compaction via Oswald ripening. More uniform nanograins produced during ball milling may retain their nanosize during the hot-press processing.

In comparing the transport properties of the NC bulk samples with those of the SOA ingot, it is important to note the relatively slow increase in k as a function of temperature for the NC bulk samples (Fig. 2D). This increase indicates a smaller bipolar contribution (2) to the conductivity by thermally generated electrons and holes in the NC bulk materials. We explain this reduced bipolar effect by assuming the existence of an interfacial potential that scatters more electrons than holes. Past studies in Bi_2Te_3 -related materials suggested that structural defects, such as antisites (i.e., Bi atoms go to Te sites), serve as an important doping mechanism (14, 15). We anticipate that such antisites are more likely to occur at interfaces. Uncompensated recombination centers at interfaces associated with defect states and antisites are responsible for charge buildup at grain boundaries and thus increase the hole density in the grains. This explanation is consistent with the observed increase in the electrical conductivity as well as the reduction in the Seebeck coefficient of the NC bulk samples, as compared with those properties of the SOA ingot parent material (Fig. 2, A and B). We modeled the transport properties based

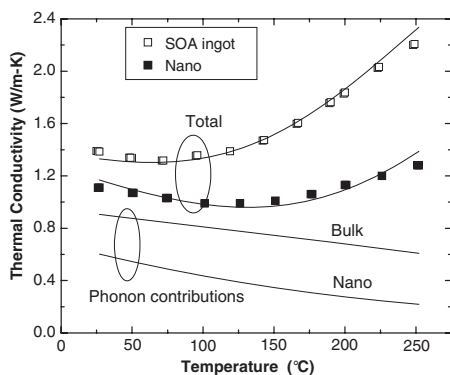


Fig. 4. Thermal conductivity of $\text{Bi}_x\text{Sb}_{2-x}\text{Te}_3$ NC bulk alloy. White and black squares represent the experimental results for an SOA ingot and our NC bulk alloys, respectively. Solid lines represent the corresponding calculations of the total (top curves) and lattice (bottom curves) contribution to the thermal conductivity, respectively.

on the Boltzmann equation within the relaxation time approximation, including the interfacial potential, and we thus obtained the lattice contributions to the thermal conductivity shown in Fig. 4. The modeled results show that phonon contributions to the lattice thermal conductivity are reduced by a factor of two.

Cooling devices. To further confirm the ZT values, we constructed two unicouple cooling devices to measure their maximum temperature difference. One unicouple uses a nanostructured p-type material as one leg and a commercially available n-type material as the other leg (Fig. 5A). The performance of this unicouple was compared with that of a second unicouple made of commercially available n- and p-type materials from the same vendor. Testing was performed in a cryostat chamber with a typical pressure of 10^{-3} torr, so that the hot-side temperature could be controlled by a combination of a heater and a continuous

flow of liquid nitrogen. Figure 5B shows the temperature difference created at different current injection levels when the hot side is maintained at 100°C . The inset displays the temperature differences created by the two devices at different hot-side temperatures. The temperature differences created with the unicouple made of commercially available p-type material are consistent with values given in the vendor catalog, whereas the performance of the unicouple made of nanostructured p-type material is significantly better. Device modeling via the measured properties is consistent with our experimental results.

Conclusion. We have developed a nanostructuring approach, and we have demonstrated significant improvement in ZT in p-type BiSbTe NC bulk alloys. The value of ZT starts at 1.2 at room temperature, peaks to 1.4 at 100°C , and decreases to 0.8 at 250°C . Such ZT characteristics are attractive for both cooling and low-temperature

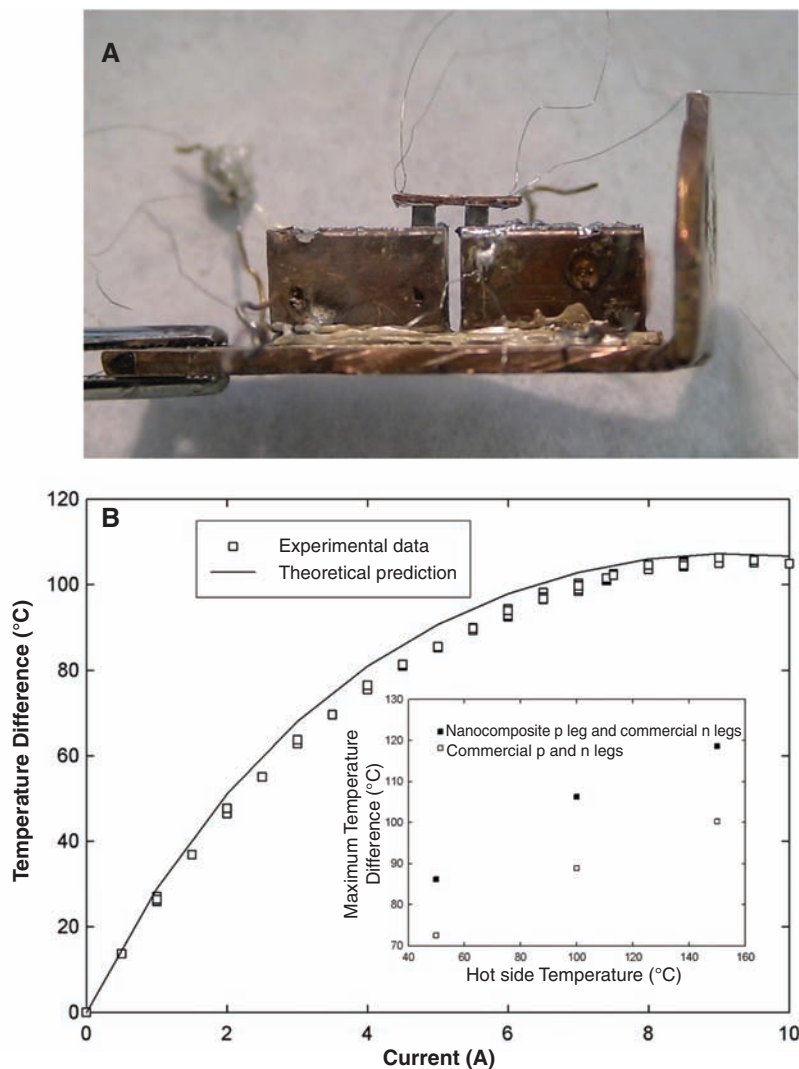


Fig. 5. (A) Experimental setup of the device cooling test. Two thermoelectric legs were mounted onto 6.5-mm-thick copper blocks and then bridged by a top copper plate. Two cold-side thermocouples were soldered into small holes drilled on both ends of the top copper plate. Hot-side thermocouples were soldered on the edge of each copper block. (B) Cooling test results with the hot side fixed at 100°C . The inset compares the maximum temperature difference of two unicouples with hot-side temperatures set at 50° , 100° , and 150°C .

waste-heat recovery applications. These materials are synthesized via ball milling, followed by dc hot pressing. The ZT enhancement comes mainly from a large reduction in the phonon thermal conductivity but also benefits from a reduction of bipolar contributions to the electronic thermal conduction at high temperatures. In the past, ZT enhancements have been reported in superlattice structures because of phonon thermal conductivity reduction. Our study suggests that a similar mechanism can be reproduced in random nanostructured bulk materials. Unlike superlattices and bulk crystals, a nanostructured BiSbTe alloy displays nearly isotropic ZT values. We further confirmed ZT enhancements by measuring the temperature difference created by uniaxial devices constructed out of the materials for hot-side temperature maintained between 50° to 150°C. The nanostructure synthesis method that we developed is a low-cost technique and can be readily scaled for mass production. These results provide a cost-effective means to improve the performance of thermoelectric materials.

References and Notes

1. D. M. Rowe, Ed. *CRC Handbook of Thermoelectrics* (CRC, Boca Raton, FL, 1995).
2. H. J. Goldsmid, *Thermoelectric Refrigeration* (Plenum, New York, 1964).
3. T. M. Tritt, Ed. *Semiconductors and Semimetals, Recent Trends in Thermoelectric Materials Research: Part One to Three* (Academic, San Diego, CA, 2001), vol. 69 to 71.
4. R. Venkatasubramanian, E. Siivola, T. Colpitts, B. O'Quinn, *Nature* **413**, 597 (2001).
5. T. C. Harman, P. J. Taylor, M. P. Walsh, B. E. LaForge, *Science* **297**, 2229 (2002).
6. K. F. Hsu *et al.*, *Science* **303**, 818 (2004).
7. J. P. Fluerial, T. Caillat, A. Borshchovsky, in *Proceedings of the 13th International Conference on Thermoelectrics*, Kansas City, MO, 30 August to 1 September 1994 (AIP, New York, 1995), pp. 40–44.
8. G. Chen, *Phys. Rev. B* **57**, 14958 (1998).
9. M. S. Dresselhaus *et al.*, *Adv. Mater.* **19**, 1043 (2007).
10. X. B. Zhao *et al.*, *Appl. Phys. Lett.* **86**, 062111 (2005).
11. X. F. Tang, W. J. Xie, H. Li, W. Y. Zhao, Q. J. Zhang, *Appl. Phys. Lett.* **90**, 012102 (2007).
12. Bulk p-type BiSbTe alloy ingots were loaded into a jar with balls inside the argon-filled glove box to avoid oxidation of the nanopowder. The jar was loaded into a ball mill and processed for several hours. When the nanopowder was ready, it was loaded into 1.25- to 2.5-cm (inner diameter) dies and compacted into a 100% dense solid NC bulk sample by a hot press. Samples are available for testing upon request.
13. We cut hot-pressed NC bulk pellets into blocks (2 mm by 3 mm by 1 mm) that were ground down into smaller blocks (2 mm by 3 mm by 0.002 mm) using a mechanical tripod polisher. We then glued the sample to a copper grid and milled it using a precision ion polishing system (Gatan Inc., Warrendale, Pennsylvania, USA) for 30 min, with incident energy of 3.2 kV and beam current of 15 μ A at an incident angle of 3.5°.
14. T. C. Harman, S. E. Miller, H. L. Goeing, *Bull. Am. Phys. Soc.* **30**, 35 (1955).
15. T. Thonhauser, G. S. Jeon, G. D. Mahan, J. O. Sofo, *Phys. Rev. B* **68**, 205207 (2003).
16. The work is supported by the U.S. Department of Energy (DOE) grant no. DE-FG02-00ER45805 (Z.F.R.), DOE grant no. DE-FG02-02ER45977 (G.C.), NSF–Nanoscale Interdisciplinary Research Team grant no. 0506830 (G.C., Z.F.R., and M.S.D.), National Science Foundation of China project no. 50528203 (J.M.L. and Z.F.R.), and the Ministry of Science and Technology of China project no. 2006CB921802 (J.M.L.). G.C. and Z.F.R. are cofounders of GMZ Energy, Inc.

13 February 2008; accepted 11 March 2008
 Published online 20 March 2008;
 10.1126/science.1156446
 Include this information when citing this paper.

REPORTS

Coherent Control of Decoherence

Matthijs P. A. Branderhorst,¹ Pablo Londero,¹ Piotr Wasylczyk,¹ Constantin Brif,² Robert L. Kosut,³ Herschel Rabitz,² Ian A. Walmsley¹

Manipulation of quantum interference requires that the system under control remains coherent, avoiding (or at least postponing) the phase randomization that can ensue from coupling to an uncontrolled environment. We show that closed-loop coherent control can be used to mitigate the rate of quantum dephasing in a gas-phase ensemble of potassium dimers (K_2), which acts as a model system for testing the general concepts of controlling decoherence. Specifically, we adaptively shaped the light pulse used to prepare a vibrational wave packet in electronically excited K_2 , with the amplitude of quantum beats in the fluorescence signal used as an easily measured surrogate for the purpose of optimizing coherence. The optimal pulse increased the beat amplitude from below the noise level to well above it, and thereby increased the coherence life time as compared with the beats produced by a transform-limited pulse. Closed-loop methods can thus effectively identify states that are robust against dephasing without any previous information about the system-environment interaction.

Interference is one of the hallmarks of quantum physics, and its presence is generally taken to demarcate the boundary between quantum and classical behavior. Controlling a quantum system consists of manipulating the relative amplitudes and phases of different distinct quantum states of the system, in order to achieve some objective, such as a particular functional operation or an increased yield of a particular outcome. The map from the optimal set of controls to the interference pattern of quantum probability amplitudes, which generates the desired outcome,

is typically very complex. Therefore, iterative adaptive control (1), in which the system is incorporated into a feedback loop, is one of the most powerful tools for optimizing quantum control results in the laboratory. This method has wide currency and is applicable to a variety of very different physical and chemical systems and processes. For example, the closed-loop approach enabled the experimenters to coherently control the shape of an atomic electron's wave function (2), energy flow in a photosynthetic complex (3), polarization-sensitive photoionization channels (4), isotope-selective photoionization of molecules (5), photoisomerization of the retinal molecule in bacteriorhodopsin (6), high-harmonic generation of coherent soft x-rays (7), selective photodissociation and rearrangement of molecular bonds (8), and large-amplitude oscillations in C_{60} (9).

The effectiveness of coherent control is compromised by the coupling of the system to an uncontrolled environment, which disturbs in a random fashion the delicate quantum phases that define the state of the system. The time scales for decoherence vary widely. For example, the dephasing times for electronic dipole excitations range from the femtosecond to nanosecond regime, as a result of coupling to local phonon modes and spontaneous emission; those for spin (magnetic-dipole) excitations vary from microseconds to milliseconds, resulting from coupling to other spins in the sample or from collisions.

Typically, the quantum system is prepared in an initial state by the controller. The system then undergoes some free evolution, during which it is affected by the environment: Both loss of quantum coherence and dissipation of energy may occur. The inability to sustain the phase and amplitude relationships between the eigenstates of the system renders the controls ineffective. Any realistic goal for quantum control therefore requires sustaining the coherence in the system, and it is an open question whether and how this is possible in the face of dephasing perturbations. In particular, is there an optimal strategy to counter the effects of the environment? Protecting the quantum coherence is an important goal in various systems and processes. For example, it was recently discovered (10) that the coherence of excited electronic states plays an important role in biochemical processes, such as energy harvesting in photosynthesis. Similarly, the coherence of multiparticle superposition states is crucial for the implementation of quantum information processing (11, 12). It is in this context that the control of decoherence has been studied most com-

¹Clarendon Laboratory, University of Oxford, Parks Road, Oxford OX1 3PU, UK. ²Department of Chemistry, Princeton University, Princeton, NJ 08544, USA. ³SCSolutions, 1261 Oakmead Parkway, Sunnyvale, CA 94085, USA.

*To whom correspondence should be addressed. E-mail: walmsley@physics.ox.ac.uk